View metadata, citation and similar papers at core.ac.uk

brought to you by CORE

provided by City Research Online

City Research Online

City, University of London Institutional Repository

Citation: Ponnusami, S. A., Turteltaub, S. and van der Zwaag, S. (2015). Cohesive-zone modelling of crack nucleation and propagation in particulate composites. Engineering Fracture Mechanics, 149, pp. 170-190. doi: 10.1016/j.engfracmech.2015.09.050

This is the accepted version of the paper.

This version of the publication may differ from the final published version.

Permanent repository link: http://openaccess.city.ac.uk/21672/

Link to published version: http://dx.doi.org/10.1016/j.engfracmech.2015.09.050

Copyright and reuse: City Research Online aims to make research outputs of City, University of London available to a wider audience. Copyright and Moral Rights remain with the author(s) and/or copyright holders. URLs from City Research Online may be freely distributed and linked to.

City Research Online: http://openaccess.city.ac.uk/ publications@city.ac.uk

Cohesive-zone modelling of crack nucleation and propagation in particulate composites

Sathiskumar A Ponnusami, Sergio Turteltaub, Sybrand van der Zwaag

Faculty of Aerospace Engineering, Delft University of Technology, Kluyverweg 1, 2629 HS Delft, The Netherlands

Abstract

A cohesive-zone approach is used to study the interaction between an approaching crack and a particle embedded in a matrix material as a function of the mismatch in elastic and fracture properties. Crack-particle interaction is a crucial issue governing fracture behavior of particle-dispersed materials. Special attention is given in the present work to the effect of the mismatch in fracture properties, namely fracture strength and energy, which has not been fully-explored in the literature. Based on extensive finite element simulations using cohesive elements, the basic fracture mechanisms governing the crack-particle interaction are identified, namely particle fracture, crack deflection and interface debonding. The details of the cracking sequences are elucidated and the role of secondary cracks is highlighted. The effect of pre-existing flaws on the fracture behavior is analyzed both for flaws inside the particle as well as flaws on the particle/matrix interface. Several flaw configurations in terms of size, orientation and location are considered. In addition, the effect of the mismatch between the matrix and the interface fracture properties is also considered for a wide range of adhesive characteristics. The results of the simulations are summarized in the form of several fracture maps for different configurations, whereby the main fracture mechanisms are identified in regions inside a two-dimensional space of strength and toughness mismatch between the particle and the matrix. It is observed that the mismatch in the fracture properties usually plays a more dominant role on the crack trajectory than the mismatch in elastic properties in a particle-dispersed system. Pre-existing flaws/defects in the particle and the interface are found to be one of the principal controlling factors that alter the crack propagation characteristics. These results can be used as a guideline for designing particulate composite system with a preferred fracture mechanism, namely matrix cracking, interface debonding or particle fracture.

1. Introduction

Particulate composites is an important class of heterogeneous materials in which the secondary phase are particles, embedded in a suitable matrix material. Particles are typically combined with the host matrix material to increase its functionality, particularly its effective fracture behavior. For example, hard second phase particles are dispersed in an otherwise homogeneous material to strengthen it. An illustrative example of material strengthening is a metal matrix reinforced with ceramic particles (see, e.g.,[1–3]). Conversely, soft ductile particles are dispersed in a brittle matrix to enhance its fracture toughness such as metallic particles dispersed in a ceramic matrix (see, e.g., [4, 5]). More recently, a distinct mechanism using embedded particles has been proposed to enhance the long term resistance against failure. In particular, in the so-called self-healing materials, particles containing a suitable healing agent are dispersed in the matrix [6, 7]. Upon loading the material, existing microcracks interact with the healing particles, thereby activating the self-healing mechanism. In order to successfully trigger the healing mechanism, it needs to be ensured that a propagating crack gets attracted towards the healing particles instead of deflecting away from them.

The fracture behavior in heterogeneous materials strongly depends on how cracks interact with the individual constituent phases at the microstructural level. In the aforementioned examples, a critical issue is the effect that a

Email addresses: S.AnusuyaPonnusami@tudelft.nl (Sathiskumar A Ponnusami), S.R.Turteltaub@tudelft.nl (Sergio Turteltaub), S.vanderZwaag@tudelft.nl (Sybrand van der Zwaag)

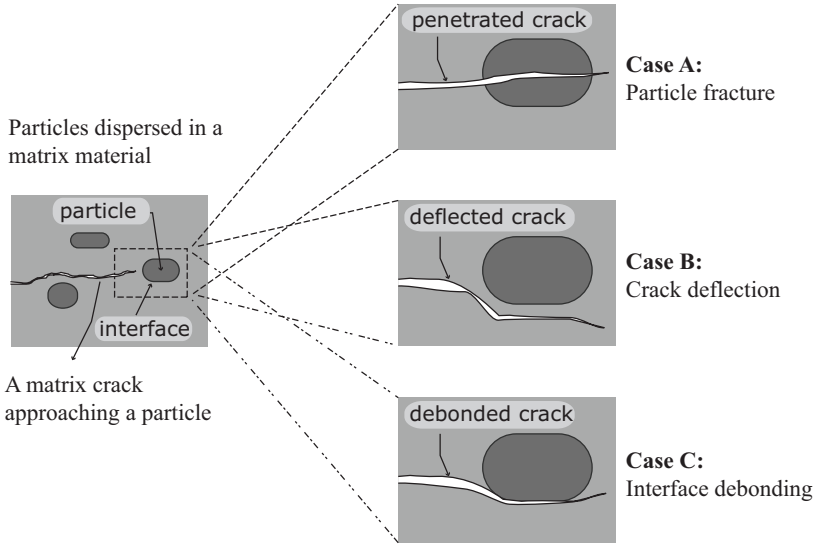

Figure 1: Crack-particle interaction in a particulate system showing three possible fracture mechanisms, namely particle fracture, crack deflection and interface debonding.

particle has on a nearby crack running through the matrix, henceforth referred to as *crack-particle interaction*. A key aspect that governs this interaction is the change in crack tip driving force due to the presence of a particle, which in turn depends upon the mismatch in the properties of the particle and the matrix. Shielding effect is observed when the particle is stiffer than the surrounding matrix material and amplification effect is observed if the particle is softer. As a consequence, a change in the crack trajectory occurs in the presence of particle. In the context of a particulate composite system, three basic fracture mechanisms could be identified, namely particle fracture, crack deflection and interface debonding as depicted in Fig. 1.

Several analytical studies have been performed to address the issue of a crack interacting with particles [8–14]. The basic goal of all those studies is to quantify the effect of the particle on the crack tip driving force through parameters like stress intensity factor (SIF) or energy release rate (ERR). The studies establish a key conclusion, namely that a reduction in SIF or crack driving force occurs if the particle ahead of the crack tip is stiffer than the surrounding material and an amplification of crack driving force occurs in the presence of a softer particle leading to shielding and antishielding effects respectively. With the advent of finite element (FE), boundary element (BE) and other numerical methods, studies have been carried out to further analyze crack-particle interaction [15–25]. The advantage of the numerical methods is that it is possible to consider more complex scenarios where analytical solutions are not feasible, such as irregular particle shapes and distribution of particles [20, 26], the presence of an additional interphase layer between the particle and the matrix [18] or the presence of pre-existing interface flaw [17].

In general, the primary focus of the aforementioned studies has been the mismatch in elastic properties between the particle and the matrix, generally supporting the notion that a crack in the matrix deflects away from a stiffer particle (shielding effect). In most studies, particle fracture was not considered or was restricted along a specified plane [24]. However, experimental observations have shown that particle fracture may occur instead of crack deflection despite the higher stiffness of the particle, which indicates that the mismatch in elastic properties is not sufficient to predict crack-particle interaction [27–30]. Hence, in the present work, one of the primary goals is to take into account additional factors that play a significant role in predicting crack-particle interaction, in particular,

- the effect of the mismatch in *fracture* properties (i.e., mismatch in fracture strength and fracture energy),
- the effect of interfacial properties (i.e., interfacial strength and toughness) and
- the influence of flaws inside the particle and on the interface.

The factors taken into account in the present study are not only important at the level of crack-particle interaction (microscale), but in fact they play a crucial role in determining the *overall* (macroscopic) fracture behavior of a

particulate system. For example, in the case of ductile matrix reinforced with brittle particles, the effective composite strength depends on the efficiency of stress transfer across the particle/matrix interface, which in turn depends on the interface strength. Hence, the material can be significantly weakened if the bonding between the particle and matrix is relatively weak [31]. In the case of ductile particles dispersed in a brittle matrix, fracture toughness enhancement is generally achieved through plastic deformation of the ductile particles. In that case, the interface properties play a vital role in facilitating the toughness improvement. For example, experimental observations show that the improvement in fracture toughness may not be realized in such systems [32–34], which is attributed to a weak particle/matrix interface, whereby the approaching crack induces debonding instead of plastic deformation in the particle. In some other cases, where both phases are brittle, relatively weak interfaces may be preferred since the interface failure can be used as an energy-dissipating mechanism, thereby enhancing the effective toughness of the material [35].

The presence of pre-existing flaws in the interface or the particle can also largely affect the fracture behavior of the particle/matrix system. For instance, Bush [17] observed that a pre-existing interface flaw can attract the approaching crack, which otherwise gets deflected. In case of brittle particle reinforced ductile matrix composites, one would expect an increase in the effective strength due to the strong brittle particles. However, brittle particles may contain flaws or defects which may be inherent to the particle itself or produced during processing. In such cases, the particles attract the approaching crack leading to substantial increase in the crack driving force, thereby resulting in degradation in strength [29]. Fracture of stiffer particles dispersed in a softer matrix are observed in several cases, which in general should have the tendency of deflecting the approaching crack [36]. Such fracture of stiffer/brittle particles is attributed to presence of flaws within the particle.

Numerical simulations have been carried out to study the behavior of a crack impinging on a planar interface [37] as well as the effect of strength of particle/matrix interface [38] or the presence of flaws on the crack path in a particulate system [39]. However, there is a need for a systematic analysis where all the relevant mechanisms (i.e., matrix cracking, particle fracture and interface debonding) are simultaneously considered, while taking into account of the mismatch in the elastic and the fracture properties between the constituent phases. Such analysis should also consider the possible nucleation, propagation and coalescence of secondary cracks as the main crack approaches a particle, since this mechanism is often critical in predicting the actual crack-particle interaction.

In the present work, a cohesive zone modelling approach is adopted [40, 41], whereby secondary cracks may nucleate in the matrix and/or the particle. Possible crack coalescence and crack bifurcations are also taken into account, which extends the range of possible interactions analyzed. Effects of the mismatch in the elastic and the fracture properties of particle, matrix and interface are examined in detail, combined with the presence of flaws both in the particle and the particle/matrix interface. For each combination of parameters and for each configuration, the crack advancement mechanism is studied and the type of crack-particle interaction is classified. The intention is to provide guidelines that can be used for analysis and design, e.g., to find the required combination of particle/matrix/interface properties to achieve a desired behavior (e.g., to enhance the effective toughness, to increase the effective strength or to trigger a self-healing mechanism).

The paper is organized as follows. The Cohesive Zone Model (CZM) adopted in the present study is summarized in Sec. 2. In addition, that section includes information about the finite element implementation and the simulation set-up. The effect of the mismatch in fracture properties between the matrix and the particle is treated in Sec. 3. The effect of pre-existing flaws in the particle is analyzed in Sec. 4. Sec. 5 addresses the influence of *interfacial* fracture properties and the presence of flaws in the interface between the particle and the matrix. Concluding remarks are provided in Sec. 6.

2. Modelling of crack-particle interaction

Classical methods in fracture mechanics may be classified as strength-based or fracture energy-based. In the strength-based approach, a crack is initiated if a stress measure (e.g., maximum principal stress) exceeds a critical value corresponding to the strength of the material. In the energy-based approach, a pre-existing crack is propagated if an energy-based measure exceeds a critical value (e.g., fracture energy). Linear elastic fracture mechanics (LEFM) methods based on strain ERR and J-integral are commonly-used energy-based approaches that quantify the amount of energy available at the crack tip for crack propagation [42]. Among these methods, the J-integral approach for fracture became very popular because it circumvents the need to resolve the crack tip stress field accurately. In general, a strength-based approach is effective for crack initiation studies whereas an energy-based approach is useful

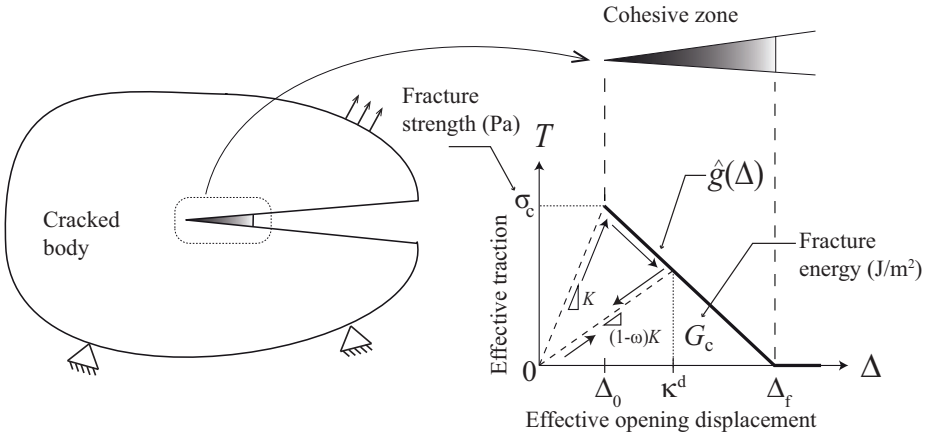

Figure 2: Cohesive zone and traction-separation law. The arrows in the traction separation law represent loading, damage, unloading and reloading steps.

for the analysis of crack propagation [43]. Most of the crack-particle interaction studies in the literature discussed in Sec. 1 adopt energy-based approaches as the key interest lies in the interaction of a propagating crack with the particle, rather than just crack initiation.

LEFM-based approaches are typically developed for studying the growth of a single pre-existing crack, hence it is in general not possible to model crack nucleation (nucleation of new cracks throughout the analysis) or coalescence of two or more cracks. In this context, Cohesive Zone Models can serve as an alternative to the strength and the energy-based approaches and they are naturally capable of overcoming these limitations. CZM combines the strength and energy-based approaches through the use of a traction-separation law [40]. Moreover, the CZM framework is naturally suitable for analyzing complex crack patterns that arise from multiple crack initiation and coalescence. In the intrinsic cohesive element-based approach adopted in the present study, nucleation, propagation and coalescence do not require additional criteria and in principle do not increase the complexity of the analysis.

2.1. Cohesive zone model and finite element implementation

In the CZM approach, the crack tip singularity predicted by the LEFM theory is replaced by a fracture process zone (the cohesive zone) where the material surface degrades from fully-coherent to complete separation. The constitutive behavior in the cohesive zone is described using a traction-separation relation as illustrated in Fig. 2, which shows the connection between a cracked body and the constitutive relation. The concept of CZM for fracture mechanics was originally developed by Barenblatt [40] for studying cracks in brittle materials and later extended to elastoplastic materials, based on related work by Dugdale [41] (see, e.g., [44]). Various cohesive laws have been proposed in the literature for different material systems such as polymers, metals and composites [44–48]. Those include exponential, polynomial, trapezoidal and bilinear traction-separation laws.

The cohesive law illustrated in Fig. 2 corresponds to a bilinear relation between T, which is a scalar measure of the traction $\boldsymbol{t}$ transmitted across the cohesive surface, and Δ, which is a scalar measure of the cohesive surface opening displacement vector $\boldsymbol{\delta}$. A bilinear relation captures the essential ingredients of most cohesive laws, namely that the traction T increases with increasing cohesive surface opening displacement Δ up to a maximum value given by the material fracture strength, σ_c, and eventually decreases to zero, at which point the cohesive zone is fully-separated in the sense that no (positive) traction can be transmitted across the surface.

The initially increasing part of the curve, which serves the purpose of modelling crack nucleation without a separate nucleation criterion, should in general have a sufficiently large slope to mimic an undamaged surface inside a material (typically referred to as a "rigid" surface in the context of cohesive relations). The initial slope K shown in Fig. 2 (i.e., the cohesive stiffness) is not a parameter that may be experimentally measured but, rather, a convenient modelling tool that is normally chosen sufficiently large compared to a representative elastic stiffness of the bulk material (e.g., Young's modulus E).

The area under the traction-separation curve, which represents the total work per unit area expended in creating a fully-separated crack, corresponds to the fracture energy (also called here as toughness for convenience) G_c of the material. Thus, both the strength and the fracture energy are simultaneously taken into account in a cohesive law used for fracture analysis. Furthermore, the cohesive zone approach introduces an inherent characteristic length to the model, designated as the cohesive zone length or fracture process zone length (FPZ), a parameter that combines elastic and fracture characteristics of a material. The fracture process zone length l_{fpz} is conventionally defined as

$$l_{\text{fpz}} := \frac{EG_c}{\sigma_c^2} \,, \tag{1}$$

where E is a representative elastic modulus of the material (typically Young's modulus for an isotropic, homogeneous material). The fracture process zone length (cohesive zone length) can be used as a measure of the brittleness of a material, with decreasing values corresponding to higher brittleness (i.e., lower ductility to strength ratio). Cohesive zone models can reproduce LEFM conditions if the fracture process zone length is negligible compared to the crack length [37], but may also be used in situations where LEFM is not applicable. The influence of fracture process zone length within the context of crack-particle interaction will be explored in later sections.

For completeness and in order to introduce the required notation, the cohesive zone model used in the present analysis is briefly summarized below [49, 50]. The traction-separation law relates the traction $\boldsymbol{t}$ acting on the crack faces, with components (t_n, t_s), to the crack opening vector $\boldsymbol{\delta}$, with components (δ_n, δ_s), where the subscripts "n" and "s" refer to the directions normal and tangential to the crack face, respectively. An effective crack opening Δ can be defined as

$$\Delta := \sqrt{\langle \delta_n \rangle^2 + \gamma^2 \delta_s^2} \,, \tag{2}$$

where $\langle \cdot \rangle = (\cdot + |\cdot|)/2$ refers to the Macaulay bracket and γ is a non-dimensional weighting factor for the mode I and mode II contributions. In order to determine whether the crack opening is increasing or decreasing due to the external loading process, the following loading function f^d is used:

$$f^d = \hat{f}^d(\Delta, \kappa^d) := \Delta - \kappa^d \,, \tag{3}$$

where $\kappa^d = \kappa^d(t)$ is a damage history variable that, at a given time t, corresponds to the maximum value attained by the equivalent crack opening during a process up to that time. The loading and unloading conditions correspond to the Karush–Kuhn–Tucker relations, see Fig. 2.

The equivalent crack opening Δ is used to compute the equivalent traction T as

$$T = \hat{T}(\Delta, \kappa^d) = \begin{cases} \hat{g}(\Delta) & \text{if} \quad f^d = 0 \text{ and } \dot{\kappa}^d > 0, \\ \\ \hat{g}(\kappa^d)\dfrac{\Delta}{\kappa^d} & \text{otherwise,} \end{cases} \tag{4}$$

where $\hat{g}$ is the effective traction-separation law and $\dot{\kappa}^d$ indicates the (time) rate of change of the damage history variable. The upper and lower expressions in (4) provide the equivalent traction during, respectively, crack growth and unloading/reloading. Alternatively, one could work with a damage variable ω and consider a "damaged" stiffness such that $(1 - \omega)K = \hat{g}(\kappa^d)/\kappa^d$ as indicated in Fig. 2. The specific form of the effective traction-separation law used in the present work is a linear softening relation (see Fig. 2), which corresponds to

$$g = \hat{g}(\Delta) = \sigma_c \frac{\langle \Delta_f - \Delta \rangle}{\Delta_f - \Delta_0} \,. \tag{5}$$

The initially linearly "elastic" loading up to the fracture strength in a bi-linear law can be reproduced in (4) by assigning an initial damage $\kappa^d(0) = \kappa_0^d = \Delta_0$. The parameter Δ_f is chosen such that the integral of $\hat{T}$ from $\Delta = 0$ to $\Delta = \Delta_f$ equals the material fracture toughness G_c, i.e., $\Delta_f = 2G_c/\sigma_c$. After evaluating (4), the normal and shear tractions can be computed such that $\boldsymbol{t} \cdot \boldsymbol{\delta} = T\Delta$ for $\delta_n \geq 0$, see [50].

In the context of the finite element method, cohesive laws can be implemented using cohesive elements [49, 51]. Cohesive elements are interface finite elements with zero thickness and their constitutive response during cracking

is given by a cohesive law. The term "interface" here refers to the fact that they are embedded between the conventional solid elements (in two or three dimensions), whereby their nodes are shared (see Fig. 5). In the present work, cohesive elements are employed for fracture studies in a particle/matrix system, in conjunction with a bilinear traction-separation law, as shown in Fig. 2.

The cohesive model presented above can be reproduced with the one available in the Finite Element package Abaqus using an appropriate choice of model options and parameters [52]. In particular, let $\delta_{n,0}$ and $\delta_{s,0}$ denote, respectively, the crack opening at the onset of failure for pure mode I and pure mode II and let $t_{n,c}$ and $t_{s,c}$ be the corresponding values of the cohesive strength, with $t_{n,c} = K\delta_{n,0}$ and $t_{s,c} = \gamma^2 K\delta_{s,0}$. The non-dimensional weighting factor γ is

$$\gamma = \frac{\delta_{n,0}}{\delta_{s,0}} ,$$

hence $\Delta_0 = \delta_{n,0} = \gamma\delta_{s,0}$ and, using the stiffnesses K and $\gamma^2 K$ in modes I and II, respectively, then $\sigma_c = t_{n,c} = t_{s,c}/\gamma$. Complete loss of cohesion occurs for pure mode I and II, respectively, at $\delta_{n,f}$ and $\delta_{s,f}$, with $\Delta_f = \delta_{n,f} = \gamma\delta_{s,f}$. The features indicated above for the linear softening model can be reproduced in Abaqus using (i) a quadratic nominal strain damage initiation criterion with $\delta_{n,0} = \gamma\delta_{s,0}$ and (ii) an energy-based linear softening model for damage evolution with an exponent equal to 1 in the power law and with equal toughness in pure mode I and II, i.e., $G_{Ic} = G_{IIc}$. Although this formulation does not contemplate distinct values of the fracture toughness in modes I and II, it has the advantage of being thermodynamically admissible since it satisfies the entropy inequality upon application of the Coleman-Noll procedure [49].

The cohesive element-based approach can be straightforward if the actual (or possible) crack path(s) is (are) known a priori. However, in general the crack path is an outcome of the simulation, hence it has to be ensured that a crack can initiate at *any* material point and can grow along an *arbitrary* direction. To this end, in the present analysis, cohesive elements are embedded along *all* continuum elements, as shown schematically in Fig. 5. For the sake of clarity, the cohesive elements are shown to possess certain thickness, but in the actual finite element mesh, they have zero thickness. To achieve the cohesive element insertion, a Matlab script is developed which reads the Abaqus input file (nodal coordinates and element connectivity) and processes them to embed cohesive elements throughout the existing mesh by introducing the required additional nodes and altering the element connectivity accordingly. One of the natural questions that arise with this methodology is the issue of mesh dependency since the crack path is still constrained to move along the element boundaries. This issue is analyzed in Appendix A for the present simulations where it is shown that, with a sufficiently refined and randomly-oriented mesh, a pre-defined mesh of cohesive elements is a viable alternative to other methods (in particular, the extended finite element method, XFEM), albeit at an increased computational cost. One key advantage of using embedded cohesive elements pertains to crack coalescence, an issue that is important in the present work, which cannot be robustly handled by the current XFEM implementation. Abaqus Standard implicit solver is used for the simulations with the standard Newton-Raphson method. To alleviate convergence difficulties (encountered during the cracking process, especially during multiple cracking and coalescence), a small value of viscosity equal to 1.0×10^{-5} s is used for the simulations.

2.2. Simulation set-up

In order to analyze the crack-particle interaction, numerical simulations are carried out in a two-dimensional rectangular domain of length L and height W, which contains a single particle of diameter $d = 2r$ embedded in a matrix. The domain contains an initially straight edge crack of length a with its crack tip located at a horizontal distance b and vertical distance c measured from the center of the particle, as shown in Fig. 3. The initial crack length is taken as $a = 0.4L$. The horizontal distance is chosen as $b = 7r$, which is sufficiently large such that the influence of the particle on the crack driving force is initially negligible, regardless of the vertical offset c (see [17, 18]). Distinct values of the offset c are considered in the analysis since this initial configuration is relevant for the subsequent crack-particle interaction. It is worth pointing out that a pre-existing crack is in principle not required for an analysis based on cohesive elements. However, for the purpose of comparing distinct crack-particle interactions, it is convenient that all simulations start with the same main approaching crack. Nevertheless, possible nucleation of secondary cracks is permitted throughout the simulation.

The specimen is loaded nominally in opening mode. A concurrent multiscale type of approach is adopted in order to eliminate the interaction between the applied load on the boundary and the stress fields in the region of interest,

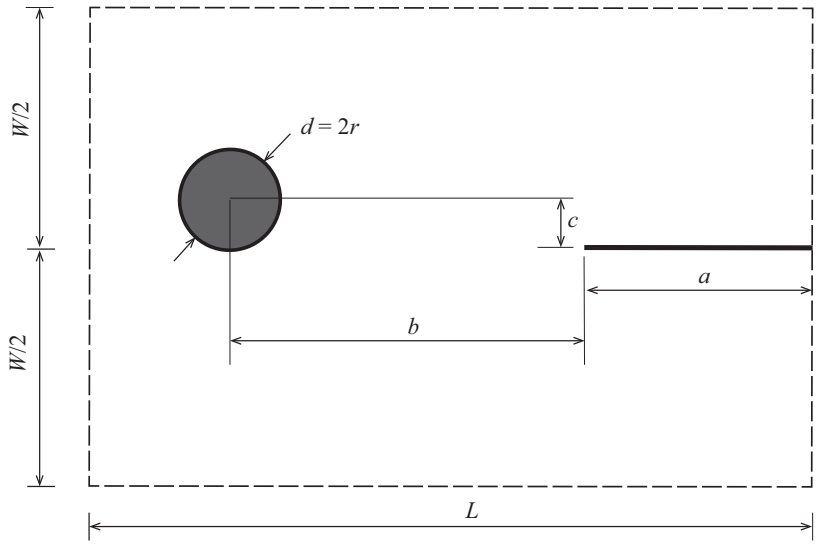

Figure 3: Particle of diameter $d = 2r$ embedded in a rectangular domain $L \times W$ with an edge crack of length $a = 0.4L$; Sketch not to scale, actual dimensions are chosen as $L = 800r$ and $L = 1.2W$. A main approaching crack tip is initially located at a horizontal distance $b = 7r$ and vertical distance c (offset).

i.e., in the proximity of particle. An infinite matrix is simulated using a two-scale finite element domain consisting of a fine mesh in the smaller inner domain containing the particle and a coarse mesh in the outer domain as shown in Fig.4. The characteristic length of the elements in the fine mesh are chosen sufficiently small compared to the fracture process zone length given in (1) in order to guarantee a proper resolution of the process zone. The dimensions of the computational domain are chosen sufficiently large compared to the radius r of the particle (in particular, $L/r = 800$ with $L = 1.2W$). Linear plane strain triangular elements are used for the continuum description and four-noded, zero thickness cohesive elements, available in the finite element package Abaqus, are used for fracture. Isotropic, linearly elastic models are used for the matrix and the particle prior to fracture.

An extensive parametric analysis is performed by considering distinct mismatches of the fracture properties, namely the strength ratio σ_c^p/σ_c^m and the toughness ratio G_c^p/G_c^m, where the superscripts "p" and "m" refer to the properties of the particle and the matrix, respectively. In addition, the interface between the particle and the matrix is modelled with a separate traction-separation relation, which depends on an (interface) strength σ_c^i and a (delamination) toughness G_c^i. Unless otherwise indicated, the properties of the matrix for the simulations are set as follows:

$$E^m = 150 \text{ GPa} , \quad \sigma_c^m = 300 \text{ MPa} , \quad G_c^m = 100 \text{ J/m}^2 .$$

For simplicity, the Poisson's ratios of the particle and the matrix, ν^p and ν^m, are kept constant and equal in all the simulations, with $\nu^p = \nu^m = 0.25$. Unless explicitly mentioned, the simulations are carried out with a ratio $E^p/E^m = 3$, which corresponds to a stiffer particle, with E^p representing the Young's modulus of the particle.

Table 1: Summary of geometric and material parameters used in this study.

Geometric parameters	Ratio of material parameters
Particle offset, ($r/2$, r, $3r/2$, $2r$)	Elastic modulus, ($E^p/E^m = 3, 1, 1/3$)
Particle flaw size, ($r/4$, $r/2$, r, $4r/3$)	Fracture strength, ($0.1 < \sigma_c^p/\sigma_c^m < 10$)
Particle flaw orientation, (0°, 30°, 60°, 90°)	Fracture toughness, ($0.01 < G_c^p/G_c^m < 100$)
Interface flaw size (angle subtended by the flaw), (15° - 120°)	Fracture process zone length, ($\bar{l}_{fpz}^m \sim 10^m, m = -1, 0, 1, 2, 3$)
Interface flaw location, (top, middle, bottom)	

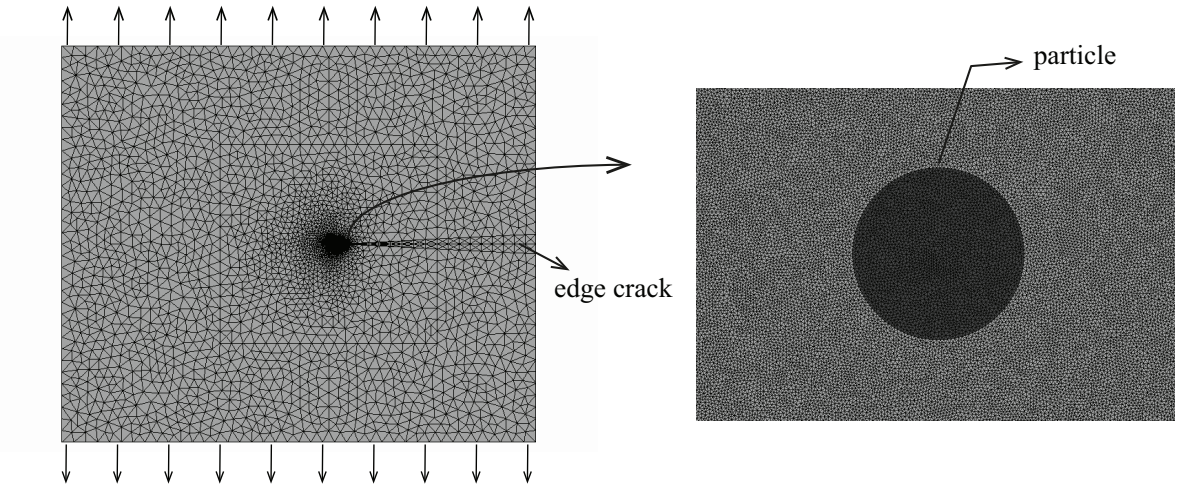

Figure 4: Two-scale finite element mesh of the complete 2D domain (left). Finer mesh near the proximity of the particle (right).

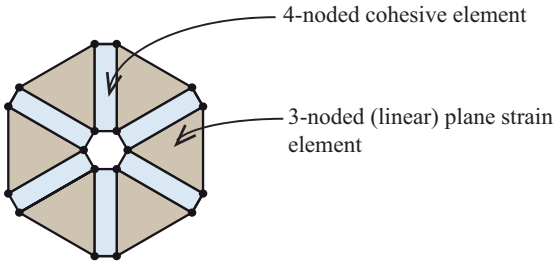

Figure 5: Schematic of embedded cohesive elements.

It is convenient to introduce in the simulations a non-dimensional fracture length scale parameter $\bar{l}^{\mathrm{m}}_{\mathrm{fpz}}$ that relates the fracture process zone length of the matrix $l^{\mathrm{m}}_{\mathrm{fpz}}$ to the particle's radius r, i.e., from (1),

$$\bar{l}^{\mathrm{m}}_{\mathrm{fpz}} := \frac{l^{\mathrm{m}}_{\mathrm{fpz}}}{r} = \frac{E^{\mathrm{m}} G^{\mathrm{m}}_{\mathrm{c}}}{(\sigma^{\mathrm{m}}_{\mathrm{c}})^2\, r} \,. \tag{6}$$

The fracture process zone length of the particle varies accordingly with the change in properties of the particle relative to the matrix. In the analysis, the radius of the particle is chosen as $r = 15\,\mu\mathrm{m}$. Along with the properties of the matrix mentioned above, the matrix fracture length scale parameter becomes $\bar{l}^{\mathrm{m}}_{\mathrm{fpz}} = 1.1 \times 10^1$. The dependance of the fracture mechanism on the length scale is explored in Sec. 4, whereby different orders of magnitude for the length scale parameter are considered by altering the toughness of the matrix. To provide an overview of the parametric simulations, different parameters and their range considered for the present study are summarized in Table 1.

The non-dimensional weighting factor γ for the mode I and mode II contributions is set to 1 (equal contribution), which implies that the simulations allow for a substantial mode II contribution if required by the local stress/deformation fields during crack growth. This is particularly relevant when analyzing interface delamination.

3. Effect of mismatch in fracture properties for a perfectly-bonded, undamaged particle

One primary goal of the present analysis is to study the effect that the mismatch in fracture properties has on the crack trajectory. To achieve this, extensive parametric analyses are conducted and the results are reported in this section. Sec. 3.1 provides the overview of different parameters used for the parametric study and describes the associated fracture mechanisms. Secs. 3.2 and 3.3 focus on the local fracture mechanisms in detail using the observed crack sequence and path, whereas Secs. 3.4 and 3.5 summarize the results of the parametric analyses in the form of fracture maps distinguishing the fracture mechanisms.

3.1. Simulation parameters and crack patterns (fracture mechanisms)

To this end, the fracture properties of the particle are varied relative to the properties of the matrix, i.e., different ratios of the fracture strengths, σ_c^p/σ_c^m, and fracture energies, G_c^p/G_c^m, are considered. In this section, the particle is assumed to be perfectly bonded to the matrix, i.e., the interfacial strength σ_c^i and the delamination toughness G_c^i are artificially set to a sufficiently large value such that separation at the particle/matrix interface is prevented. All the simulations conducted in Sec. 3 are obtained with the fracture length scale of the matrix, $\bar{l}_{fpz}^m = 1.1 \times 10^1$. The fracture length scale of the particle varies accordingly with its elastic and fracture properties relative to the matrix.

In addition to distinct fracture properties, it is also relevant to consider different crack-path offsets c as indicated in Fig. 3. Four representative values are considered for c, namely $c = r/2, r, 3r/2$ and $2r$, which are within the range of practical interest in which the interaction between the crack and the particle is noticeable as the main crack approaches the particle. For each set of fracture properties and offset, a numerical simulation is carried according to the set-up indicated in Sec. 2.2 and the corresponding crack pattern is classified in terms of one of the following possible outcomes:

- **Case 1**: Particle fracture, which occurs either when the main approaching crack enters into the particle or when a secondary crack nucleates inside the particle and grows into the matrix.
- **Case 2**: Crack deflection, which corresponds to the situation where the main approaching crack remains confined to the matrix.

Observe that the notion of particle fracture is reserved in the present work for a situation where a crack runs continuously across the particle/matrix interface. In other words, if a new secondary crack initiates inside the particle or a secondary crack initiates from a pre-existing flaw within the particle, but does not propagate into the matrix, then the fracture mechanism is not qualified as particle fracture. Further, the expression crack "deflection" refers to the fact that the crack does not enter the particle, regardless of whether the initial offset c is increased or reduced. The relevance of the classification indicated above is connected to the purpose of embedding particles in the matrix. In particular, case 1 is typically required when designing a particle-based self-healing material whereas case 2 is often favorable for particle toughening purposes.

Numerical simulations, using the model parameters indicated in Sec. 2.2, are carried out by increasing the remotely-applied external load (see Fig. 4) until the crack tip has moved substantially away from the particle, at which point the crack pattern close to the particle is not expected to evolve further. In order to get insight into the crack-particle interaction, crack paths are shown and discussed in detail for two selected particle offsets, $c = r/2$ and $3r/2$, for representative mismatches in fracture properties and for two mismatches in elastic properties, namely $E^p/E^m = 3$ (stiff particle) and $E^p/E^m = 1/3$ (soft particle). A summary of calculations for all offsets is provided at the end of this section.

3.2. Behavior of incoming cracks aligned with particle (offset $c = r/2$)

An initial crack offset $c = r/2$ (see Fig. 3) is representative of the situation where the particle is located directly in front of the path of an incoming crack. The actual path that the crack adopts as it approaches the particle depends on the relative elastic and fracture properties of the matrix and the particle, as shown in Fig. 6. Figures on the left column (a,c, and e) correspond to a stiffer particle case, $E^p/E^m = 3$ and figures on the right column (b, d and f) correspond to softer particle case, $E^p/E^m = 1/3$. The other relative properties (i.e., the relative fracture strength and toughness) are varied correspondingly and shown in the figure. In all cases, the particle is initially undamaged and has a perfect bonding with the matrix.

All crack paths shown in Fig. 6, which advance from right to left, are essentially the same until the crack front reaches a distance equal to the diameter of the particle (measured from the particle's center). In three cases (a, b and f) particle fracture is observed whereas in the other cases (c, d, and e), crack deflection occurs. Small crack fluctuations in the crack paths may in fact be attributed to mesh resolution (see also Appendix A). It can be observed from Fig. 6a and b that, when there is no mismatch in fracture properties (same fracture properties for the particle and the matrix), particle fracture occurs in both cases, however, the stiffer particle (case a) deflects the incoming crack away from it. Nonetheless, the mismatch in elastic modulus does not prevent particle fracture despite higher stiffness of the particle.

When the strength of the particle is larger than the strength of the matrix while the toughnesses are the same (cases c and d), the approaching crack deflects along the particle. It is worth indicating that the crack actually does

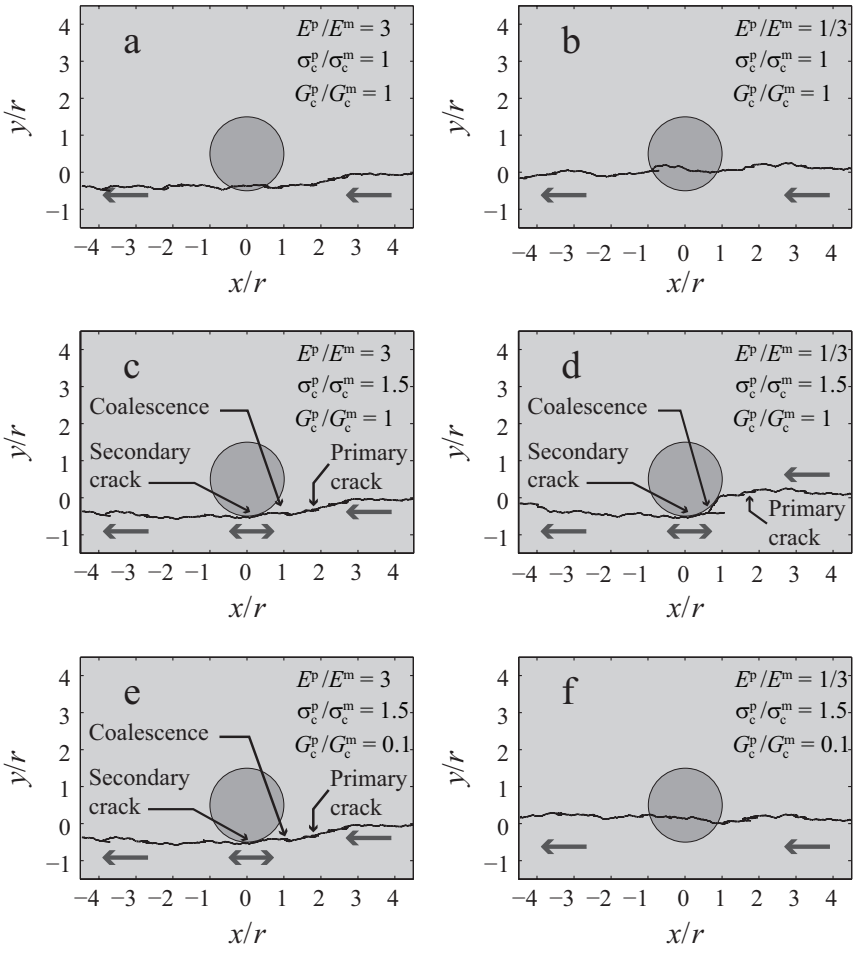

Figure 6: Crack paths of an incoming crack with an initial offset $c = r/2$ relative to a perfectly-bonded, undamaged particle for selected mismatches in elastic and fracture properties (advancing crack path is from right to left).

not propagate monotonically. Instead, as the primary crack approaches the particle, a secondary crack nucleates near the bottom of the particle (on the matrix side). This secondary crack grows and eventually coalesces with the primary incoming crack. Subsequently, after effectively by-passing the particle via this mechanism, the unified crack resumes its mode I path in the matrix. The crack paths shown in the figures only indicate the parts that are open (portions of the secondary crack that are closed due to unloading are not shown). Consequently, it can be concluded that for cases c and d, the mismatch in fracture properties have a significant influence on the crack path.

Cases e and f show the interplay between elastic and fracture properties, which show a more significant effect of the mismatch in elastic modulus. In these cases, the strength of the particle is higher than the matrix (as in cases c and d), but the toughness of the particle is smaller (reduced by a factor of 10 relative to the toughness of the matrix). Case e is essentially similar to the case c indicated above (i.e., a secondary crack nucleates and coalesces with the main crack). In case f the main crack is attracted to the particle due to the elastic mismatch (soft particle). This behavior is initially similar to case d, however in case f the toughness of the particle is relatively low and the main crack continues through the particle. Hence, the mismatch in elastic properties do play a significant role in cases e and f, but only in combination with the fracture properties.

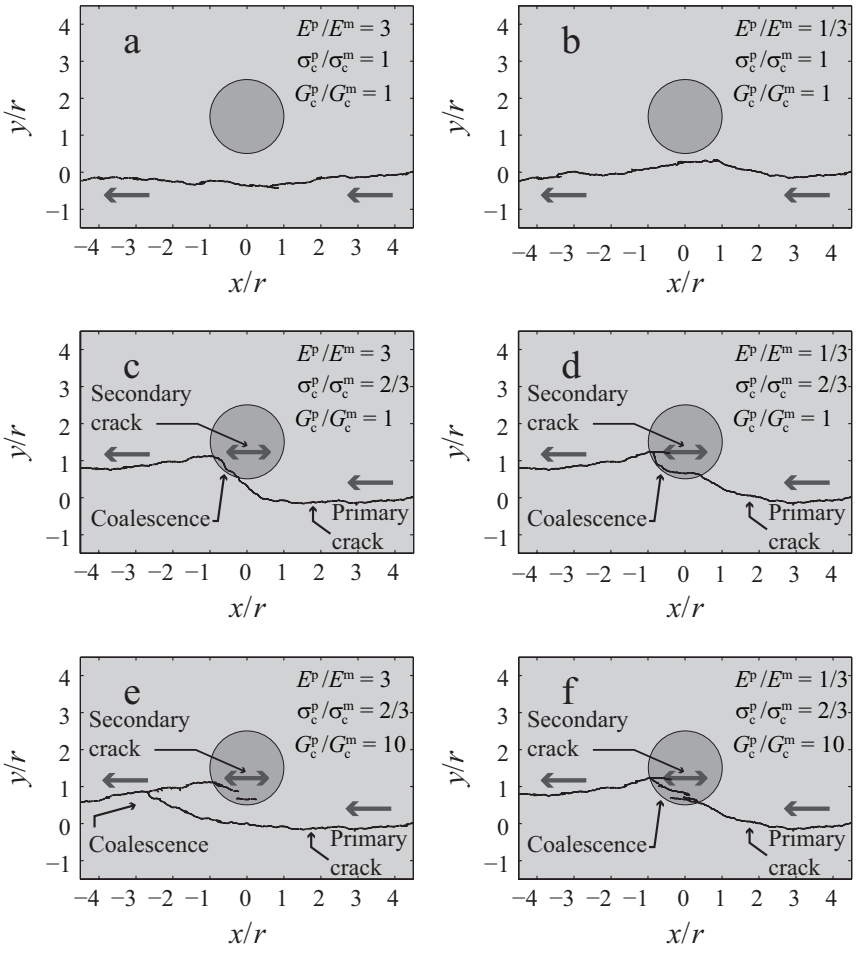

Figure 7: Crack paths for particle offset $c = 3r/2$; crack path is from right to left.

3.3. Behavior of incoming cracks not aligned with particle (offset $c = 3r/2$)

Representative crack paths for an incoming crack with an offset $c = 3r/2$ with respect to the particle are indicated in Fig. 7. The crack paths on left side of the figure correspond to the stiffer particle case ($E^p/E^m = 3$) and the right side corresponds to the softer particle case ($E^p/E^m = 1/3$). As in Sec. 3.2, all crack paths are essentially the same until the crack front reaches a distance equal to the diameter of the particle. In two cases (a and b) crack deflection occurs whereas in the other cases (c, d, e and f), particle fracture occurs.

In cases a and b in Fig. 7 the fracture strength and toughness are the same for the particle and the matrix, hence any deviation from a straight path can be purely attributed to the elastic modulus mismatch. For the stiffer particle, case a, a slight crack deflection away from the particle is observed. In case b, the main crack is attracted towards the softer particle. The elastic mismatch (lower stiffness of the particle), however, is not sufficiently low to completely deviate the crack path, which eventually moves away from the particle due to the influence of the externally applied stress field.

Cases c and d shown in Fig. 7 correspond to a *weaker* particle, where the strength of the particle is 2/3 of the strength of the matrix. It is interesting to note from these figures that for both the stiffer and the softer particle cases, a secondary microcrack nucleates inside the particle due to the stress field of the main approaching crack and eventually both cracks coalesce. Some small differences can be observed between cases c and d in Fig. 7 (stiffer and softer

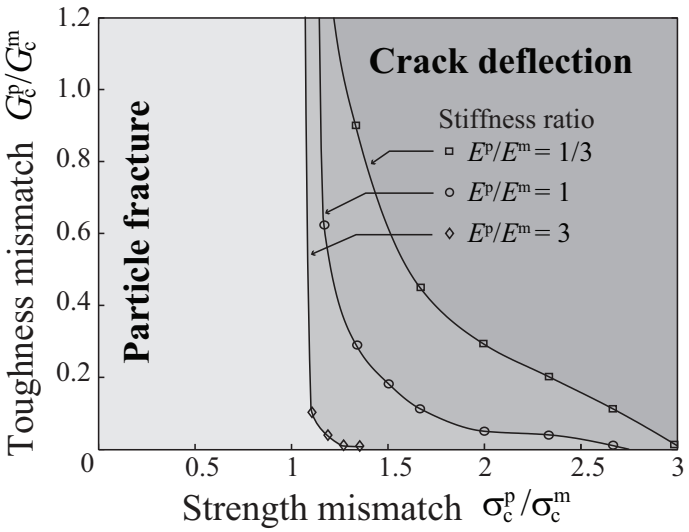

Figure 8: Fracture map: Effect of mismatch in elastic properties. Three stiffness ratios are considered corresponding to stiffer particle, particle with same stiffness of the matrix and softer particle. The curves shown are obtained for an offset $c = r/2$. The transition curves correspond to the boundary separating the regions in which particle fracture or crack deflection occurs, as a function of the strength mismatch σ_c^p/σ_c^m and the toughness mismatch G_c^p/G_c^m.

particle cases), where it can be seen that the main crack gets attracted towards the softer particle earlier than the stiffer particle. This is due to the fact that, in case of a stiffer particle, only the (lower) strength makes the crack change its direction towards the particle, whereas in case of a softer particle, both the stiffness (tendency of softer particle attracting a crack) and the lower strength play a role in the crack path. Despite these differences, the effect of the elastic mismatch is relatively unimportant in these cases, when it comes to the fracture mechanism.

In cases e and f in Fig. 7, crack paths are reported in which the toughness of the particle is one order of magnitude higher than the toughness of the matrix, while the particle strength is kept lower, as in cases c and d. Comparing cases e and f with the corresponding cases c and d, it can be observed that increasing the fracture energy (toughness) does not prevent the deflection of the main crack towards the particle. One notable difference between cases e and f is that for the stiffer particle (case e), the main crack coalesces with the secondary crack in the matrix, after it has passed the particle, whereas coalescence occurs inside the particle in case f. This difference can be attributed to the mismatch in elastic properties (in case f, the softer particle further attracts the main crack).

Based on the results shown in Sec. 3.2 and Sec. 3.3, it can be concluded that a purely energy-based fracture mechanics approach, which cannot consider the mismatch in strength, would fail in capturing relevant fracture scenarios since it could not account for a secondary crack initiation. Thus, a purely energy-based criteria may over-emphasize the role of the mismatch in elastic properties in predicting crack paths. The effect of the mismatch in elastic properties is not discussed in detail as it has been explored extensively in the literature. However, for completeness, the effect of the mismatch in elastic properties is analyzed in the following section within the context of the current framework that accounts for both strength and toughness.

3.4. Effect of mismatch in elastic properties: fracture map

The influence of the elastic mismatch is analyzed by considering three different modulus ratios, namely $E_p/E_m = 3, 1$ and $1/3$. In all cases, the main approaching crack has an initial offset of $c = r/2$ (i.e., the particle lies directly in front of the path of the primary crack). The results of a large number of simulations is conveniently summarized in the form of a fracture map (i.e., failure-mechanism map), as shown in Fig. 8. For each mismatch in elastic properties, the corresponding curve shown in Fig. 8, called a *transition* curve, separates the regions of the fracture strength σ_c^p/σ_c^m and fracture toughness G_c^p/G_c^m for which an approaching crack would either break the embedded particle or not. In particular, the regions to the left and bottom of a curve correspond to particle fracture and the regions to the right and

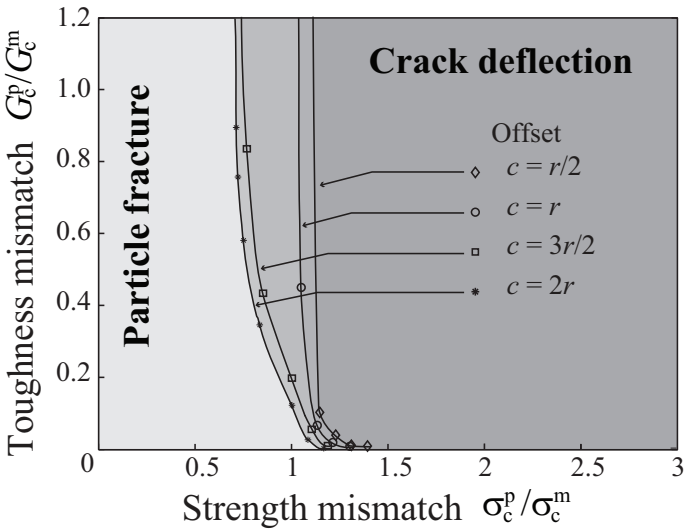

Figure 9: Fracture map for a perfectly-bonded, undamaged particle: Effect of particle offset. The curves shown are obtained for the stiffness ratio, $E^p/E^m = 3$. For four distinct initial offsets c, the curves shown correspond to the boundary separating the regions in which particle fracture or crack deflection occurs, as a function of the strength mismatch σ_c^p/σ_c^m and the toughness mismatch G_c^p/G_c^m.

top of the curve correspond to crack deflection. In order to determine the curves shown in Fig. 8, a large number of simulations need to be carried out to identify the corresponding strength and fracture energy ratios where the transition from case 1 to case 2 occurs (the curve itself is an interpolation between the properties of the nearest points where the transition is observed). It should be noted that, for each mismatch in elastic properties, a single transition curve was identified in the fracture map.

The general trend is that particle fracture is favored with a decrease in stiffness of the particle. This is qualitatively in accordance with a general conclusion established in the literature that indicates that a softer particle attracts the approaching crack and a stiffer particle deflects the approaching crack away from it. However, the fracture behavior is significantly dependent upon the mismatch in fracture properties as seen in Fig. 8. It is also observed that the interplay between the mismatch in fracture strength and toughness is more pronounced for softer particles (e.g., $E_p/E_m = 1/3$) than for stiffer particles (e.g., $E_p/E_m = 3$). It is interesting to note that particle fracture occurs in case of softer particle, even if the fracture strength of the particle is higher that that of the matrix by a factor of 2 or even more, provided the fracture toughness of the particle is sufficiently low. In case of stiffer particle, particle fracture is precluded if the strength of the particle is higher by a factor of 1.3 relative to the matrix strength, irrespective of lower fracture toughness of the particle.

3.5. Fracture maps for a perfectly-bonded, undamaged particle

Similar to the results presented in the previous section, it is convenient to summarize the results of a large number of simulations for distinct offsets c. In this case, the mismatch in elastic properties is set to $E^p/E^m = 3$ (stiffer particle) for all simulations.

Distinct types of transitions from one case to the other have been observed in the simulations, corresponding to distinct changes in crack patterns. Crack paths for the different offsets are not reported here, rather the fracture maps corresponding to different offsets are shown in Fig. 9. For all offsets analyzed, if the mismatch in toughness G_c^p/G_c^m is sufficiently high, the transition curves depend mostly on the mismatch in fracture strength σ_c^p/σ_c^m (i.e., all transition curves are nearly vertical for $G_c^p/G_c^m > 0.6$). Correspondingly, the mismatch in fracture strength is the deciding factor in order to predict whether particle fracture or crack deflection would occur. However, if the mismatch in toughness is sufficiently low (e.g., $G_c^p/G_c^m < 0.4$), then the transition curve is slightly influenced by this parameter. Nonetheless, for any considered offset, it is observed that particle fracture does not occur even for very low toughness of the particle, if the strength of the particle is higher than that of the matrix by a factor of 1.3.

It is worth recalling that the fracture map shown in Fig. 9 corresponds to a significantly stiff particle, relative to the matrix, with $E^{\mathrm{p}}/E^{\mathrm{m}} = 3$. It is well-known that stiffer particles tend to deflect incoming cracks. Nonetheless, it is interesting to observe that for the offset $c = r/2$, i.e., when the particle is in front of the incoming crack path, the primary matrix crack can directly break an equally stronger particle even if it is tougher and stiffer than the matrix (i.e., $\sigma_{\mathrm{c}}^{\mathrm{p}}/\sigma_{\mathrm{c}}^{\mathrm{m}} \approx 1$ for $G_{\mathrm{c}}^{\mathrm{p}}/G_{\mathrm{c}}^{\mathrm{m}} > 1$ and $E_{\mathrm{c}}^{\mathrm{p}}/E_{\mathrm{c}}^{\mathrm{m}} = 3$). Furthermore, particles can break even if they are not in the path of the incoming crack (i.e., for $c \geq r$) provided that the particle strength is sufficiently low. This situation arises when the particle is subjected to the influence of the approaching crack stress field and a secondary crack is generated inside the particle. The secondary crack may grow into the matrix and coalesce with the incoming primary crack, effectively generating particle fracture even if the primary crack does not (directly) break the particle. Hence, despite the tendency of stiffer particles to deflect incoming cracks, the influence of the elastic stiffness on the interaction between an incoming crack and the particle is in general secondary and the behavior depends mostly on the fracture properties. Elastic properties do play a role in the fracture process as discussed in previous section. Nonetheless, the point emphasized here is that for a fixed elastic property mismatch, the influence of the fracture property mismatch is much more pronounced than the considered mismatch in elastic stiffness.

4. Effect of pre-existing flaws inside the particle

In Sec. 3 it was assumed that the particle was initially undamaged. Typically, however, flaws can occur during processing of the composite material or they can be inherent to the material itself (e.g., brittle particles). As a consequence, the expected strength gain may not be achieved as these flaws can weaken the system instead of strengthening it. Thus, for practical applications, it is important to study the effect of such flaws as they may significantly affect the anticipated performance of a composite. To study the effect of pre-existing flaws on the fracture behavior, a single representative flaw, located in the center of the particle, is considered in the simulations reported in this section. The flaw is initially confined to the interior of the particle and the particle/matrix interface is assumed to be perfectly bonded (simulated with a sufficiently large interface strength).

Two main geometrical parameters of the flaw are varied in a parametric analysis, namely its initial size and its orientation with respect to the main approaching crack. All parametric analyses carried out for distinct geometrical characteristics of the flaw are obtained with the same fracture length scale of the matrix used in Sec. 3, namely $\bar{l}_{\mathrm{fpz}}^{\mathrm{m}} = 1.1 \times 10^{1}$. However, an additional parametric analysis is conducted in this section, namely for distinct values for the matrix fracture length scale $\bar{l}_{\mathrm{fpz}}^{\mathrm{m}}$, in order to investigate the effect of this quantity on the fracture behavior.

As pre-existing flaws are most often observed in stiff and brittle particles (compared to softer particles) only the stiffer particle case is considered in this section ($E_p/E_m = 3$). All the analyses are carried out for the particle offset $c = 3r/2$, which is representative of a particle that does not lie ahead of an approaching crack.

4.1. Mechanism of crack-particle-flaw interaction

To demonstrate the effect of the particle flaw and establish a link between a fracture map and a fracture mechanism, it is useful to first illustrate one representative sequence of a crack-particle-flaw interaction. A particle with a flaw of size r is shown in Fig. 10, where r is the radius of the particle. To focus on the effect of the flaw, the fracture properties for the particle and the matrix are kept the same. Upon loading, it can be observed that there are two different stress fields, one for the main crack and the other associated with the flaw inside the particle as seen in Fig. 10a. Despite the stress concentration inside the particle, the flaw does not initially grow (recall that the stress predicted using a cohesive zone approach is finite). However, once the main crack approaches the particle as shown in Fig. 10b, the two stress fields interact with each other leading to further amplification of the stresses inside the particle. Eventually a secondary crack is activated starting from the tip of the flaw. Upon further loading, the secondary crack originated from the flaw grows further and attracts the approaching main crack towards the particle, finally resulting in coalescence with the main crack as observed sequentially in Fig. 10c and Fig. 10d. This crack advancement mechanism is somewhat similar to cases studied in Sec. 3, except that the possibility of appearance of a secondary crack is increased due to the presence of the flaw. The initial location of this secondary crack is mostly dependent upon the location of the flaw. The quantitative effect of the flaws are studied in the next subsections based on flaw size and flaw orientation.

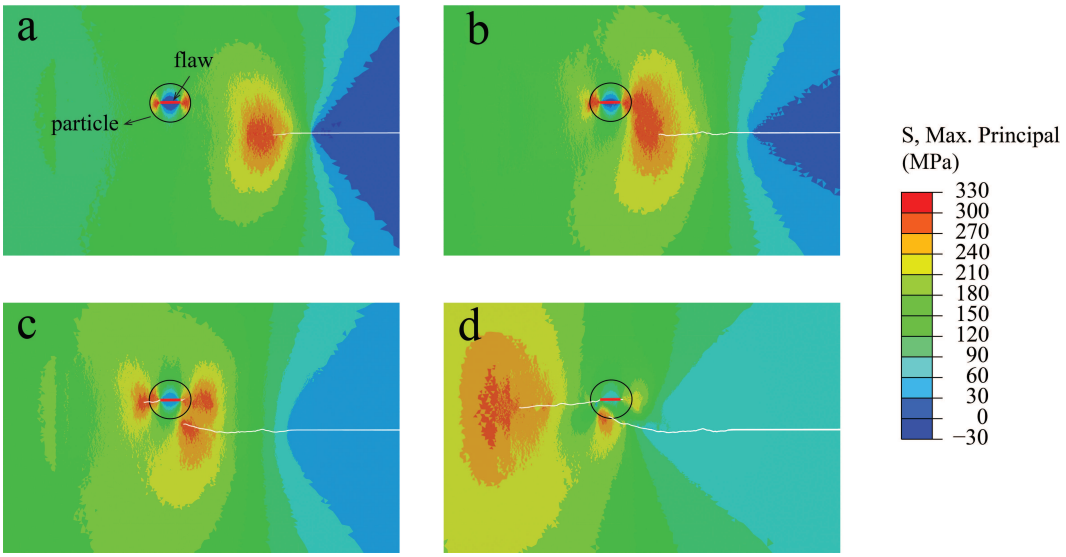

Figure 10: Crack-flaw interaction: a) two different stress fields corresponding to the flaw and the main crack, b) the initial interaction between the two stress fields, c) a secondary crack initiating from the flaw and simultaneously the main crack getting attracted towards the flaw, d) further coalescence of the flaw-induced secondary crack and the attracted main crack.

4.2. Effect of flaw size

Four different flaw sizes in the particle, namely $r/4$, $r/2$, r and $4r/3$, are considered in order to simulate the range from small to large flaws. Their effect can also be compared to the undamaged particle case studied in Sec. 3 (i.e., no flaw). The corresponding results with a crack that has an initial offset $c = 3r/2$ are shown in Fig. 11. In all cases the fracture strength and the toughness are the same for both the particle and the matrix in order to focus on the influence of the flaw. It can be observed that flaws with sizes equal to $r/4$ and $r/2$ (cases a and b) do not significantly alter the crack path compared to the case of an undamaged particle. In contrast, larger flaws, namely r and $4r/3$, have an important effect as can be observed in cases c and d in Fig. 11. Hence, these results indicate that there is a critical flaw size (in this case somewhere between $r/2$ and r), for which the crack response changes from crack deflection (case 1) to particle fracture (case 2). The critical flaw size corresponds to the minimum length for which a secondary crack can nucleate and grow from the flaw tip (i.e., there is sufficient stress concentration to both nucleate and subsequently propagate a secondary crack).

In order to globally assess the effect of flaw size on the crack path, a wide range of fracture properties of the particle relative to the matrix are considered. The results corresponding to different flaw sizes are summarized in the form of fracture maps in Fig. 12, for a representative offset, namely $c = 3r/2$. Essentially, each transition curve indicates the locus of material properties for which the flaw size is critical. As it can be clearly observed from the results, the presence of a particle flaw shifts the transition curve upwards and towards the right simultaneously (higher particle strength and toughness), favoring particle fracture with increased flaw size compared to the case with no flaw.

It is interesting to note that the fracture map curve for the no flaw case is almost vertical, implying that the failure mechanism is dominantly controlled by fracture strength only. However, if a flaw is introduced, failure is also controlled by fracture toughness, a dependency that can be traced back to the secondary crack mechanism as indicated in Sec. 4.1. In general, for sufficiently large particle toughness, the transition between particle fracture to crack deflection is dominated by the mismatch in strength (near vertical lines), while for sufficiently large particle strength, the transition is dominated by the mismatch in toughness (near horizontal curves). Nonetheless, it is worth indicating that for particles with very low relative toughness, the transition between fracture mechanisms (case 1 and 2) eventually does occur at a finite value of the strength mismatch σ_c^p/σ_c^m, albeit a large one (i.e., although not shown for the flaw sizes r and $4r/3$, the transition curves eventually intersect the horizontal axis). For intermediate cases, both strength and toughness play equally important roles. For the flaw sizes $r/4$ and $r/2$, the transition lines are very close to the one with no flaw for sufficiently large values of G_c^p/G_c^m, implying that particles may have flaws but that

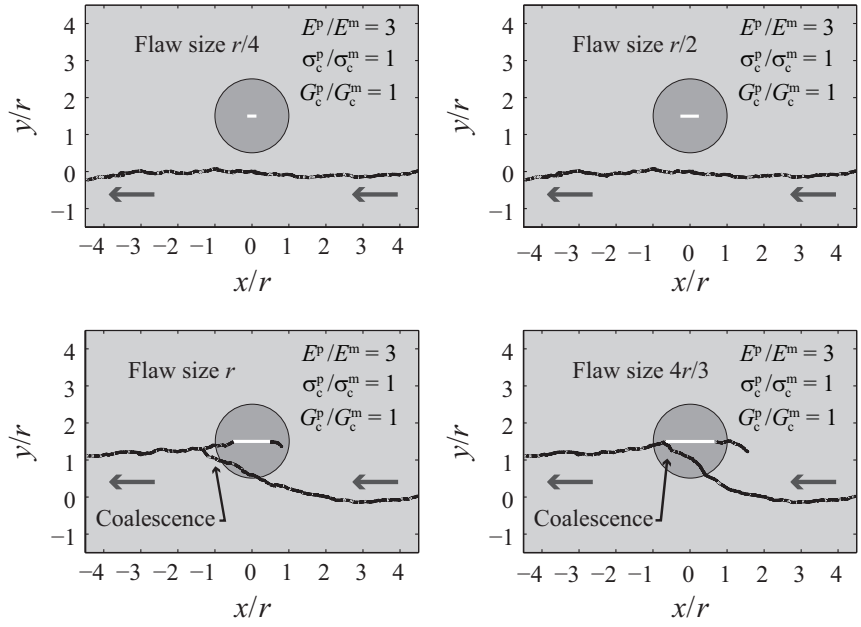

Figure 11: Crack patterns for different flaw sizes, In all cases, the particle is stiff and the particle and matrix have equal fracture properties. The crack path is from right to left.

their *effective* strength is not significantly affected if the particle toughness is sufficiently high.

4.3. Effect of flaw orientation

The results displayed in the previous section were obtained assuming that the flaw was aligned with the main incoming crack. However, typically flaws and cracks are not aligned and it is anticipated that the critical flaw size will strongly depend on the relative orientation. To quantify this assertion, for a flaw of size equal to r, different representative flaw orientations were analyzed, namely 0°, 30° , 60° and 90°, where each angle indicates the relative orientation of a flaw with respect to the incoming crack. The corresponding fracture maps are shown in Fig. 13.

Among the four different orientations analyzed, the flaw aligned with the incoming crack (i.e., 0°) is the most critical. This due to the fact that the 0°-oriented flaw is mostly loaded in mode I conditions, which favors the nucleation and growth of a secondary crack emanating from the flaw. Hence, the particle with 0° flaw will have the least resistance to particle fracture compared with the other three flaw orientations. The flaw orientation 90° corresponds to the least favorable conditions for crack nucleation and propagation. Nonetheless, even the presence of the 90°-oriented flaw can alter the crack path, provided the toughness is sufficiently low. This is because the mismatch in elastic properties and the non-symmetric stress field related to the approaching primary crack may lead to a local mixed-mode condition in which a crack can be activated in the flaw. In general, it can be concluded that the presence of a flaw clearly decreases the resistance to particle fracture; the *smallest* critical flaw size corresponds to the case where the flaw and the incoming crack are aligned.

4.4. Effect of fracture length scale parameter

Cohesive zone models contain an intrinsic fracture process zone length as defined in (1) for the matrix material. Consequently, in a particle-matrix system, it is possible to compare the size of the particle to the intrinsic matrix fracture length by introducing a fracture length scale parameter, as given in (6). The influence of this length scale parameter on the fracture behavior in the particle-matrix system is examined by considering a wide range of matrix toughnesses, namely $G_c^m = 10^n$ J/m^2, with $n = 0, 1, 2, 3, 4$, resulting, respectively, in five different length scale

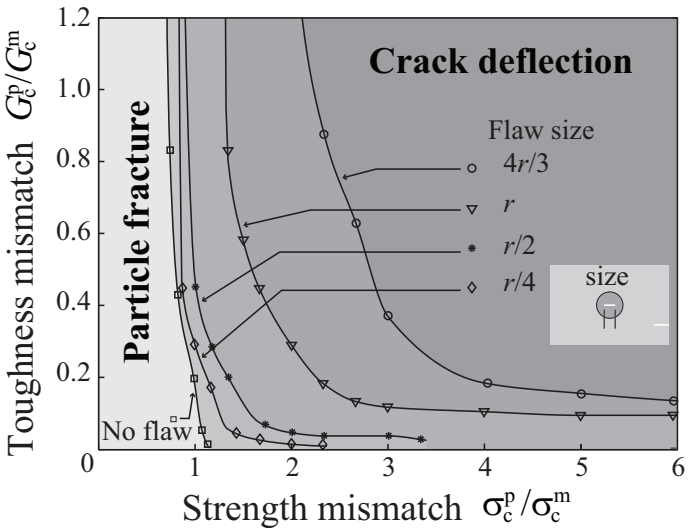

Figure 12: Fracture map: Effect of pre-existing flaws inside a perfectly-bonded particle for an offset $c = 3r/2$. The transition curves indicate the points for which the flaw size is critical and a secondary crack emanates from the flaw.

parameters, i.e., $\bar{l}^{\mathrm{m}}_{\mathrm{fpz}} = 1.1 \times 10^m$, with $m = -1, 0, 1, 2, 3$. Recall that the reference value used in the previous sections was $G^{\mathrm{m}}_{\mathrm{c}} = 10^2$ J/m^2 , which corresponds to $\bar{l}^{\mathrm{m}}_{\mathrm{fpz}} = 1.1 \times 10^1$. The simulations in this section are conducted with a flaw in the particle of size $r/2$, which is aligned with an incoming crack that has an offset $c = 3r/2$. The transition curves from particle fracture to crack deflection are plotted in Fig. 14 for each fracture length scale parameter.

From the Fig. 14, it may be observed that, when the fracture process zone length is very large relative to the particle size (i.e., $\bar{l}^{\mathrm{m}}_{\mathrm{fpz}} \gg 1$), the mismatch in fracture strength becomes the dominating factor. For example, for the length scale parameters $\bar{l}^{\mathrm{m}}_{\mathrm{fpz}} = 1.1 \times 10^2$ and $\bar{l}^{\mathrm{m}}_{\mathrm{fpz}} = 1.1 \times 10^3$, the corresponding fracture map is almost vertical, signifying that it is predominantly the mismatch in strength that plays a role in determining the point in which the fracture mechanism changes. It is worth pointing out that, for the length scale parameter, namely $l^{\mathrm{m}}_{\mathrm{fpz}}/r = 1.1 \times 10^3$, (plotted as dotted curve in the figure for the purpose of clarity) the fracture map is essentially vertical, with a transition curve defined by a single value of the strength mismatch, namely $\sigma^{\mathrm{p}}_{\mathrm{c}}/\sigma^{\mathrm{m}}_{\mathrm{c}} = 1.3$. This behavior can be explained as follows: If the length scale is very large for the matrix (hence for the particle as well, as particle fracture properties are varied relative to the matrix), then the characteristic stress field associated with such large fracture process zone involves dissipation (amount of energy spent in formation and extension of process zone) of the specified fracture energy over a very larger length of the process zone. Under such conditions, the *extension* of the *cohesive* crack tip of either the main crack in the matrix or the flaw within the particle over a considered length relative to the particle size would only require a very small fraction of the specified fracture energy of the particle and the matrix. Hence, any mismatch in fracture energy between the particle and matrix, in general, would have a negligible effect on the crack path. Consequently, the extension of the cohesive crack tip is controlled predominantly by the mismatch in the strength, resulting in vertical transition curves for very large length scales, namely $\bar{l}^{\mathrm{m}}_{\mathrm{fpz}} = 1.1 \times 10^2$ and $\bar{l}^{\mathrm{m}}_{\mathrm{fpz}} = 1.1 \times 10^3$. Furthermore, for increasing fracture length scales, it has been observed that there exists a limit for the value of strength mismatch above which particle fracture does not occur. This can be observed by comparing the nearly vertical transition curves in the Fig. 14 corresponding to the length scales, $\bar{l}^{\mathrm{m}}_{\mathrm{fpz}} = 1.1 \times 10^2$ and $\bar{l}^{\mathrm{m}}_{\mathrm{fpz}} = 1.1 \times 10^3$.

Conversely, for lower values of the length scale, toughness mismatch also plays a prominent role in deciding the fracture mechanism. This is because, if the material fracture process zone length is small relative to the particle size, the energy dissipated over the considered extension of the cohesive crack tip (of the propagating matrix crack or the crack inside the particle) becomes significant and contributes to a larger fraction of the specified fracture energy. In this case, the mismatch in fracture energy between the particle and the matrix becomes important to trigger the propagation of the pre-existing flaw within the particle. In the limit case of infinitesimally small length scale, the particle is mostly subjected to the same stress field used in linear elastic fracture mechanics, which is theoretically recovered in the

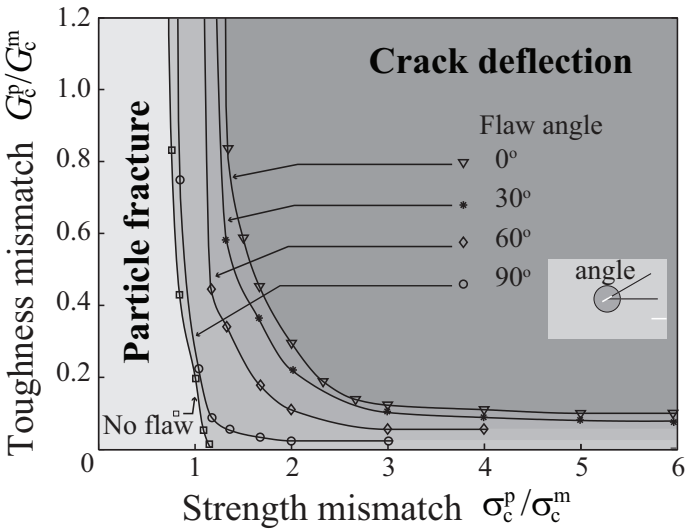

Figure 13: Fracture maps: Effect of flaw orientation for a flaw size equal to r and an initial crack offset $c = 3r/2$.

limit $\bar{l}^{\mathrm{m}}_{\mathrm{fpz}} \to 0$. In that case, it is to be expected that the energy dissipated is crucial. Thus, for intermediate and small fracture length scales, both strength and fracture energy mismatch have an effect on the fracture behavior. The results on the effect of fracture process zone length agree well qualitatively with the work of Parmigiani and Thouless [37], in the sense that the mismatch in strength is the controlling factor for larger length scales, though the problems analyzed are quite different.

5. Effect of interface fracture properties and interface flaws

In the previous sections, the bonding between the particle and the matrix was assumed to be perfect. This was modelled by assigning sufficiently high values to the interface strength $\sigma^{\mathrm{i}}_{\mathrm{c}}$ and the interfacial fracture energy $G^{\mathrm{i}}_{\mathrm{c}}$ (delamination toughness). Consequently, cracks in the vicinity of the interface could only run across or remain close to the interface. However, in many particle/matrix systems, the interface between the particles and the matrix may have a lower strength and toughness than that of the bulk materials. In some cases it is possible that no adhesion is achieved between the particle and the matrix in portions of the interface (i.e., there is an *interface flaw*). These two issues are analyzed in this section, namely the influence that the interfacial fracture properties and the presence of interfacial flaws have on the trajectory of an incoming crack.

5.1. Influence of fracture properties of the interface

The simulations in this section are carried out for a primary crack with a representative offset ($c = 3r/2$), for the reference non-dimensional value of the fracture length scale of the matrix $\bar{l}^{m}_{\mathrm{fpz}} = 1.1 \times 10^{1}$ and for a particle without an internal flaw (but possibly an interfacial flaw). To focus on the effect of the interfacial properties and flaws, the fracture properties of the particle and matrix are kept the same for all the simulations in this section. Both the stiffer ($E_p/E_m = 3$) and softer ($E_p/E_m = 1/3$) particle cases are considered. When the interface is allowed to break, a new fracture mechanism is available, namely *interface delamination*. However, for simplicity, only selected examples are shown instead of a fracture map. In particular, crack patterns when the interface strength is equal to 2/3 of the matrix strength (which is equal to particle strength), are shown in Fig. 15. The results corresponding to the stiffer and softer particle cases are shown in the left and right sides of the figure, respectively. Cases a and b are obtained with an interfacial toughness equal to that of the surrounding phases (particle and matrix), whereas in cases c and d the interfacial toughness is one order of magnitude higher.

In all cases shown in Fig. 15, a secondary crack appears at the interface and eventually coalesces with the main crack. This is in contrast to the case of perfect particle bonding (cases a and b in Fig. 7), where the crack runs in the

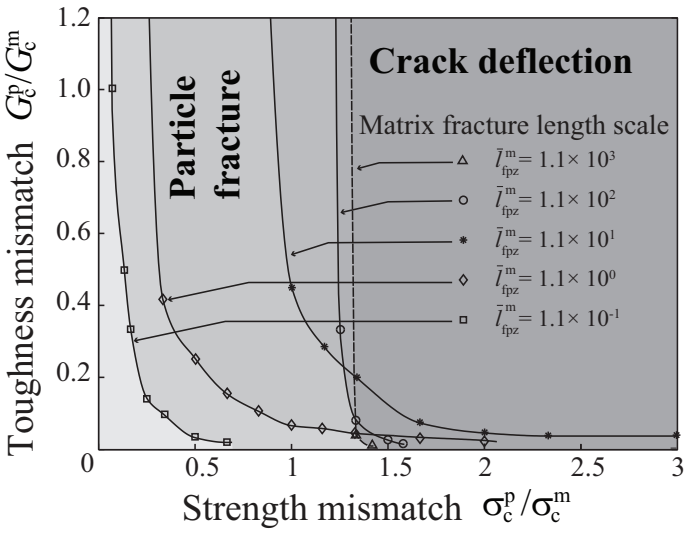

Figure 14: Fracture maps: Effect of fracture length scale parameter for a particle with a flaw of size $r/2$ and an incoming crack with an offset $c = 3r/2$.

matrix and does not reach the interface. It is relevant to observe that in the cases shown in Fig. 15, strictly speaking, the particle itself does not crack but, rather, the interface separates. Furthermore, as may be observed in cases c and d, an increase in the interfacial fracture energy does not prevent the interface from separating, which indicates that this is a phenomenon that is mostly controlled by the interfacial strength (i.e, if the interface strength is reduced below a certain limit, debonding always occurs irrespective of the interface fracture energy).

5.2. Flaw in interface

Flaws in the particle/matrix interface may be generated during processing leading to poor or no bonding in some parts of the interface. To provide insight on the consequences that this lack of bonding has on the interaction between an incoming crack and a particle, selected interfacial flaw configurations, in terms of size and their location, are considered. The simulation conditions are similar to the ones indicated in Sec. 5.1, except that the interfacial strength and toughness are chosen equal to that of the surrounding phases in order to focus on the effect of the interfacial flaw. For simplicity, only the stiffer particle case ($E_p/E_m = 3$) is considered in this section. Three representative locations of a flaw on the interface are considered, designated as bottom, middle and top, where bottom refers to the portion of the particle/matrix interface closest to an incoming crack with an offset $c = 3r/2$. Several sizes were considered for the flaws in the three aforementioned positions. In all three locations, a critical flaw size was identified such that the flaw attracts the main crack irrespective of the high strength and fracture energy for the rest of the interface (i.e., for any value of $\sigma^{i}_{c} \geq \sigma^{p,m}_{c}$ and $G^{i}_{c} \geq G^{p,m}_{c}$). The crack paths associated with the critical sizes for flaws located at the bottom, middle and top locations are shown in Fig. 16 (cases a, b and c, respectively). For flaws smaller than the critical value, the crack pattern is *qualitatively* similar to the one shown in case a in Fig. 7 (i.e., the crack runs in the matrix, similar to the perfect bonding case). The critical length is quantified in each case in terms of the angle subtended by the flaw, i.e., 15°, 120° and 90° for cases a, b and c, respectively (in which case the critical length is computed as θr, where θ is the angle measured in radians and r the radius of the particle). The smallest critical length corresponds to the bottom flaw due to its proximity to the incoming crack and the fact that it is essentially oriented in the same direction as the crack. In contrast, the largest critical length corresponds to the middle flaw, since it is not favorably oriented in order to trigger further interface debonding. The critical length for the top flaw is bounded between the smallest and the largest critical sizes analyzed; it is interesting to observe that in this case (case c in Fig. 16), the failure mechanism involves both particle fracture and debonding as the main crack traverses the particle as it coalesces with the secondary crack. In contrast, only particle debonding is observed in cases a and b.

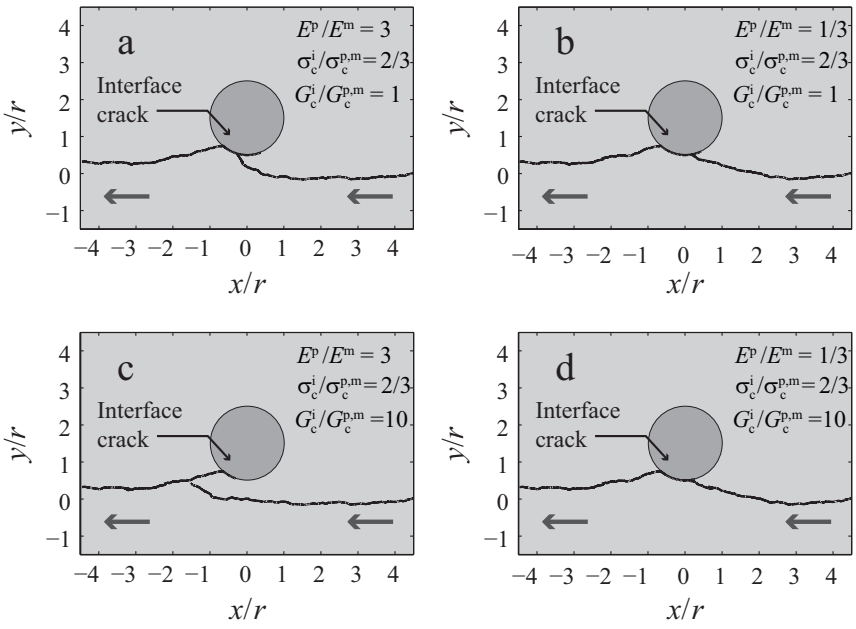

Figure 15: Crack paths for particle offset case, $c = 3r/2$: effect of interface fracture properties; crack path is from right to left.

For comparison purposes, a fourth case is included in Fig. 16, namely case d in which no flaw is present but the interfacial toughness is reduced up to a point where debonding and subsequent coalescence occurs at the bottom of the particle. This situation is similar to the crack patterns previously observed in case a in Fig. 15 and case a in Fig. 16. From these cases, it may be concluded that debonding and coalescence may be triggered due to (i) low interfacial strength, (ii) low interfacial toughness or (iii) the presence of a flaw (despite a high interfacial strength and toughness).

6. Concluding remarks

Numerical simulations using a cohesive zone model were carried out to analyze the influence that a particle embedded in a matrix has on the trajectory of a crack. Complex interactions can be observed between the crack and the particle in some cases, with an overall crack advancement composed of a sequence of nucleation, propagation and coalescence of secondary cracks in the particle or the matrix. A summary of distinct failure mechanisms (particle fracture, crack deflection and interface debonding) were reported for a wide range of combinations of fracture properties of the matrix, particle, interface and under the presence of flaws in the particle or the interface. From the simulations, the following general conclusions were drawn:

- The trajectory of a crack is primarily dependent upon the fracture properties, while elastic properties often (though not always) play a secondary role.
- The mismatch in strength between the particle and the matrix was found to be the dominant factor affecting the fracture behavior in undamaged, perfectly bonded particles. Above a critical value of the strength mismatch, crack deflection occurs regardless of the toughness mismatch.
- Toughness mismatch (i.e., mismatch in fracture energies of particle and matrix) also plays an important role in determining the crack path if flaws are present in the particle.
- The mismatch in strength is the dominant factor, even in the presence of a flaw, if the matrix cohesive zone length is sufficiently large (i.e., when the matrix material has a more ductile-like fracture behavior).

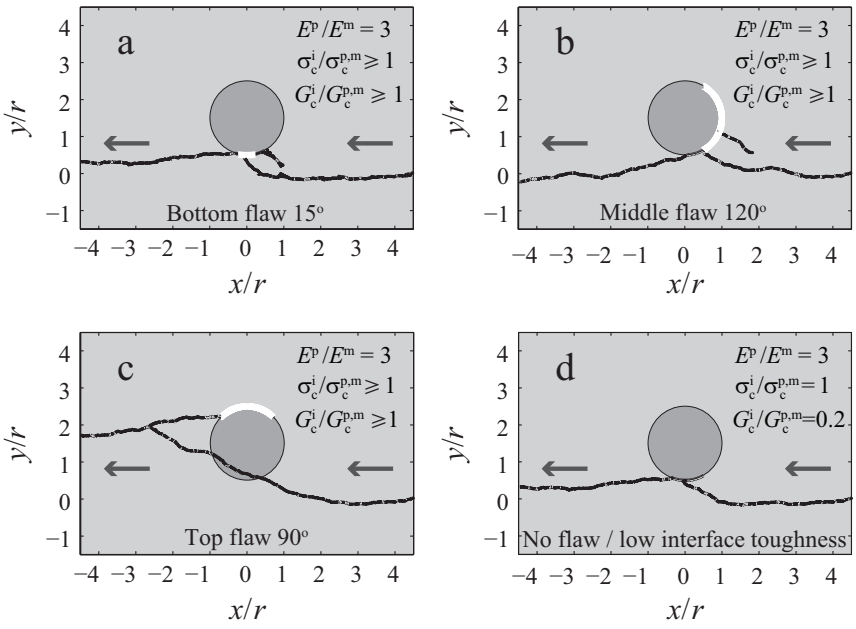

Figure 16: Effect of interface flaw on crack path; crack path is from right to left.

- The effect of fracture properties of the interface is critical in deciding the crack path. Further, presence of interface flaws highly favors debonding of the particle/matrix interface.

For design purposes, it is important to fine-tune the mismatch in mechanical properties when a given outcome is required. In particular, for particles embedded in a matrix for self-healing purposes, the present study indicates that a very good bonding between the particles and the matrix is required while, simultaneously, particles should have a sufficiently small fracture strength. With this combination, a self-healing mechanism can be successfully triggered by the incoming crack, which itself needs to the healed.

Acknowledgments

This work is part of the projects SHM01021 and SAMBA carried out by the authors along with their collaborators. We thank IOP Self Healing Materials (Agentschap NL) and European Union Seventh Framework Programme (FP7/2007-2013, grant agreement n° 309849) for their financial support of our research. We extend our sincere thanks to our collaborator Prof. W. G. Sloof for his valuable support and interactive discussions.

References

References

[1] J. Li, B. Zong, Y. Wang, W. Zhuang, Experiment and modeling of mechanical properties on iron matrix composites reinforced by different types of ceramic particles, Materials Science and Engineering: A 527 (29) (2010) 7545–7551.

[2] T. Srivatsan, Microstructure, tensile properties and fracture behaviour of Al_2O_3 particulate-reinforced aluminium alloy metal matrix composites, Journal of Materials Science 31 (5) (1996) 1375–1388.

[3] T. Christman, A. Needleman, S. Suresh, An experimental and numerical study of deformation in metal-ceramic composites, Acta Metallurgica 37 (11) (1989) 3029–3050.

[4] L. S. Sigl, P. Mataga, B. Dalgleish, R. McMeeking, A. Evans, On the toughness of brittle materials reinforced with a ductile phase, Acta Metallurgica 36 (4) (1988) 945–953.

[5] V. V. Krstic, P. S. Nicholson, R. G. Hoagland, Toughening of glasses by metallic particles, Journal of the American Ceramic Society 64 (9) (1981) 499–504.
[6] S. R. White, N. Sottos, P. Geubelle, J. Moore, M. Kessler, S. Sriram, E. Brown, S. Viswanathan, Autonomic healing of polymer composites, Nature 409 (6822) (2001) 794–797.
[7] S. Zwaag, Self healing materials: an alternative approach to 20 centuries of materials science, Springer Netherlands, 2007.
[8] C. Atkinson, The interaction between a crack and an inclusion, International Journal of Engineering Science 10 (2) (1972) 127–136.
[9] O. Tamate, The effect of a circular inclusion on the stresses around a line crack in a sheet under tension, International Journal of Fracture Mechanics 4 (3) (1968) 257–266.
[10] F. Erdogan, G. Gupta, M. Ratwani, Interaction between a circular inclusion and an arbitrarily oriented crack, Journal of Applied Mechanics 41 (4) (1974) 1007–1013.
[11] F. Erdogan, G. Gupta, The inclusion problem with a crack crossing the boundary, International Journal of Fracture 11 (1) (1975) 13–27.
[12] E. Patton, M. Santare, The effect of a rigid elliptical inclusion on a straight crack, International Journal of Fracture 46 (1) (1990) 71–79.
[13] Z. Xiao, B. Chen, Stress intensity factor for a Griffith crack interacting with a coated inclusion, International Journal of Fracture 108 (3) (2001) 193–205.
[14] Z. Li, Q. Chen, Crack-inclusion interaction for mode I crack analyzed by Eshelby equivalent inclusion method, International Journal of Fracture 118 (1) (2002) 29–40.
[15] P. Lipetzky, Z. Knesl, Crack-particle interaction in a two-phase composite Part II: crack deflection, International Journal of Fracture 73 (1) (1985) 81–92.
[16] R. Li, A. Chudnovsky, Energy analysis of crack interaction with an elastic inclusion, International Journal of Fracture 63 (3) (1993) 247–261.
[17] M. Bush, The interaction between a crack and a particle cluster, International Journal of Fracture 88 (3) (1997) 215–232.
[18] M. Knight, L. Wrobel, J. Henshall, L. De Lacerda, A study of the interaction between a propagating crack and an uncoated/coated elastic inclusion using the BE technique, International Journal of Fracture 114 (1) (2002) 47–61.
[19] R. Kitey, A.-V. Phan, H. Tippur, T. Kaplan, Modeling of crack growth through particulate clusters in brittle matrix by symmetric-Galerkin boundary element method, International Journal of Fracture 141 (1-2) (2006) 11–25.
[20] A. Ayyar, N. Chawla, Microstructure-based modeling of crack growth in particle reinforced composites, Composites Science and technology 66 (13) (2006) 1980–1994.
[21] R. Williams, A.-V. Phan, H. Tippur, T. Kaplan, L. Gray, SGBEM analysis of crack–particle(s) interactions due to elastic constants mismatch, Engineering Fracture Mechanics 74 (3) (2007) 314 – 331, ISSN 0013-7944.
[22] P. Lipetzky, S. Schmauder, Crack-particle interaction in two-phase composites Part I: Particle shape effects, International Journal of Fracture 65 (4) (1994) 345–358.
[23] M.-O. Nandy, S. Schmauder, B.-N. Kim, M. Watanabe, T. Kishi, Simulation of crack propagation in alumina particle-dispersed SiC composites, Journal of the European Ceramic Society 19 (3) (1999) 329–334.
[24] A. Ayyar, N. Chawla, Microstructure-based modeling of the influence of particle spatial distribution and fracture on crack growth in particle-reinforced composites, Acta Materialia 55 (18) (2007) 6064–6073.
[25] S. Natarajan, P. Kerfriden, D. R. Mahapatra, S. Bordas, Numerical analysis of the inclusion-crack interaction by the extended finite element method, International Journal for Computational Methods in Engineering Science and Mechanics 15 (1) (2014) 26–32.
[26] V. Romanova, R. Balokhonov, S. Schmauder, The influence of the reinforcing particle shape and interface strength on the fracture behavior of a metal matrix composite, Acta Materialia 57 (1) (2009) 97–107.
[27] J. Leggoe, X. Hu, M. Bush, Crack tip damage development and crack growth resistance in particulate reinforced metal matrix composites, Engineering Fracture Mechanics 53 (6) (1996) 873–895.
[28] D. Lloyd, Aspects of fracture in particulate reinforced metal matrix composites, Acta metallurgica et materialia 39 (1) (1991) 59–71.
[29] M. Manoharan, J. Lewandowski, Crack initiation and growth toughness of an aluminum metal-matrix composite, Acta Metallurgica et Materialia 38 (3) (1990) 489–496.
[30] J. N. Hall, J. W. Jones, A. K. Sachdev, Particle size, volume fraction and matrix strength effects on fatigue behavior and particle fracture in 2124 aluminum-SiC p composites, Materials Science and Engineering: A 183 (1) (1994) 69–80.
[31] S.-Y. Fu, X.-Q. Feng, B. Lauke, Y.-W. Mai, Effects of particle size, particle/matrix interface adhesion and particle loading on mechanical properties of particulate–polymer composites, Composites Part B: Engineering 39 (6) (2008) 933–961.
[32] K. V. Rao, W. Soboyejo, R. Ritchie, Ductile-phase toughening and fatigue-crack growth in Nb-reinforced molybdenum disilicide intermetallic composites, Metallurgical Transactions A 23 (8) (1992) 2249–2257.
[33] V. D. Krstic, On the fracture of brittle-matrix/ductile-particle composites, Philosophical Magazine A 48 (5) (1983) 695–708.
[34] X. Sun, J. Yeomans, Optimization of a Ductile-Particle-Toughened Ceramic, Journal of the American Ceramic Society 79 (10) (1996) 2705–2717.
[35] J. Yang, S. Jeng, Interface and mechanical behavior of $MoSi_2$-based composites, Journal of Materials Research 6 (03) (1991) 505–513.
[36] K. Wallin, T. Saario, K. Törrönen, Fracture of brittle particles in a ductile matrix, International Journal of Fracture 32 (3) (1986) 201–209.
[37] J. Parmigiani, M. Thouless, The roles of toughness and cohesive strength on crack deflection at interfaces, Journal of the Mechanics and Physics of Solids 54 (2) (2006) 266–287.
[38] W. Wang, K. Sadeghipour, G. Baran, Finite element analysis of the effect of an interphase on toughening of a particle-reinforced polymer composite, Composites Part A: Applied Science and Manufacturing 39 (6) (2008) 956–964.
[39] M. C. Alfaro, A. Suiker, C. Verhoosel, R. De Borst, Numerical homogenization of cracking processes in thin fibre-epoxy layers, European Journal of Mechanics-A/Solids 29 (2) (2010) 119–131.
[40] G. I. Barenblatt, The mathematical theory of equilibrium cracks in brittle fracture, Advances in applied mechanics 7 (1) (1962) 55–129.
[41] D. Dugdale, Yielding of steel sheets containing slits, Journal of the Mechanics and Physics of Solids 8 (2) (1960) 100–104.
[42] T. L. Anderson, Fracture mechanics: fundamentals and applications, CRC press, 2005.
[43] P. Cornetti, N. Pugno, A. Carpinteri, D. Taylor, Finite fracture mechanics: a coupled stress and energy failure criterion, Engineering Fracture Mechanics 73 (14) (2006) 2021–2033.

[44] V. Tvergaard, J. W. Hutchinson, The relation between crack growth resistance and fracture process parameters in elastic-plastic solids, Journal of the Mechanics and Physics of Solids 40 (6) (1992) 1377–1397.
[45] A. Needleman, An analysis of tensile decohesion along an interface, Journal of the Mechanics and Physics of Solids 38 (3) (1990) 289–324.
[46] P. H. Geubelle, J. S. Baylor, Impact-induced delamination of composites: a 2D simulation, Composites Part B: Engineering 29 (5) (1998) 589–602.
[47] A. Cornec, I. Scheider, K.-H. Schwalbe, On the practical application of the cohesive model, Engineering Fracture Mechanics 70 (14) (2003) 1963–1987.
[48] M. Elices, G. Guinea, J. Gomez, J. Planas, The cohesive zone model: advantages, limitations and challenges, Engineering Fracture Mechanics 69 (2) (2002) 137–163.
[49] M. Ortiz, A. Pandolfi, Finite-deformation irreversible cohesive elements for three-dimensional crack-propagation analysis, International Journal for Numerical Methods in Engineering 44 (9) (1999) 1267–1282.
[50] T. Hille, A. Suiker, S. Turteltaub, Microcrack nucleation in thermal barrier coating systems, Engineering Fracture Mechanics 76 (6) (2009) 813–825.
[51] X.-P. Xu, A. Needleman, Numerical simulations of fast crack growth in brittle solids, Journal of the Mechanics and Physics of Solids 42 (9) (1994) 1397–1434.
[52] ABAQUS, version 6.11 Documentation, Dassault Systemes Simulia Corp., Providence, RI, USA .
[53] Y. Mi, M. Crisfield, G. Davies, H. Hellweg, Progressive delamination using interface elements, Journal of composite materials 32 (14) (1998) 1246–1272.
[54] A. Seagraves, R. Radovitzky, Advances in cohesive zone modeling of dynamic fracture, in: Dynamic Failure of Materials and Structures, Springer, 349–405, 2010.
[55] J. J. Rimoli, J. J. Rojas, F. N. Khemani, On the mesh dependency of cohesive zone models for crack propagation analysis, in: 53rd AIAA/ASME/ASCE/AHS/ASC Structures, Structural Dynamics and Materials Conference, 2012.

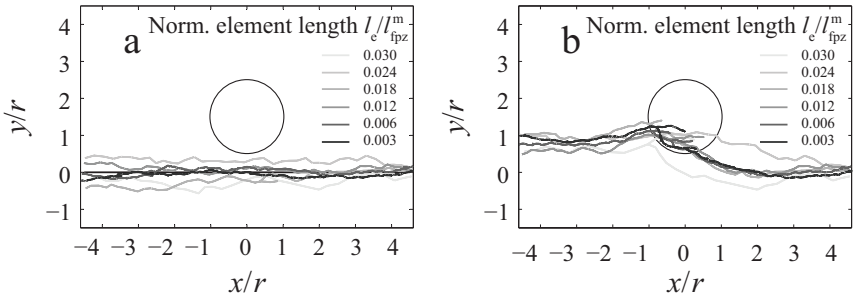

Figure A.17: Mesh convergence studies for (a) a straight crack path (homogeneous system) and (b) a deflected crack path (weaker particle). Crack path is from right to left.

Appendix A. Study on mesh dependency

In the quasi-static computational approach adopted in the present simulations, the cohesive elements are embedded within the edges of the solid elements (see Fig. 5). Correspondingly, a crack can only move along cohesive elements and the issue of mesh dependency becomes relevant. In this case, the evolution of a crack path is not associated to a kinetic law (e.g., orientation for maximum dissipation criterion), but, instead, it is naturally chosen from the cohesive elements that "break" first according to their orientation and the local stress field. To mitigate the effect of mesh dependency, a fine random mesh is generated, which allows for a good resolution of the cohesive zone (see, e.g., [53]) and, equally important, a relatively arbitrary crack propagation. In practice, the crack path direction is chosen from an equilibrium path, which means that an effective kinetic law emerges from the simulations.

An overview of mesh-dependency effects with the use of cohesive elements can be found in [54, 55]. In order to quantify the mitigating effects of a refined, random mesh in the present analysis, a mesh refinement analysis has been carried out for a fixed particle offset of $c = 3d/4$, considering two different cases. In the first case, the particle and the matrix are assumed to have the same elastic and fracture properties. Consequently, in accordance with the maximum dissipation criterion for a homogeneous linearly elastic matrix, a straight crack path is expected as a solution under remote mode I loading. Five different mesh densities are considered in the analysis and the resulting crack paths are shown in Fig. A.17a. The characteristic element length l_e, normalized with the fracture process zone length l^m_{fpz}, is used as the parameter representing the mesh density. The finest mesh used in the analysis contains 447 522 nodes and 372 824 elements, of which 223 650 are cohesive elements. In the second case analyzed, the elastic properties are kept equal, but the fracture strength of the particle is reduced by a factor of two relative to the matrix. In this case, a deflected crack path is observed, where a secondary microcrack initiates within the weaker particle and coalesces with the approaching primary crack (see Fig. A.17b).

In both cases, crack path convergence can be achieved by having a sufficiently fine mesh. For the first case, the crack paths converge to one that fluctuates about the straight path. The fluctuations are inherent to the fact that the crack is constrained to propagate only along element boundaries. In the second case, it is important to have a refined mesh for crack path convergence, since crack coalescence is only observed inside the particle once the mesh is sufficiently fine.

To further verify the convergence, the first case (straight path) is analyzed in more detail. Figure A.18 shows the differences in the crack paths corresponding to the case shown in Fig. A.17a. The error is obtained by taking an L_2 norm of the difference between the computed and the straight crack. The norm is proportional to the gray area shown schematically in the inset in Fig. A.18 and is computed in the region of interest shown in the figures (i.e., $-4 \leq x/r \leq 4$), using all the completely failed cohesive elements. It can be observed that the error over the crack path decreases with an increase in mesh density. This trend confirms that the magnitude of the fluctuations of the crack path around the straight path, decreases.

A related parameter that is relevant for monitoring convergence is the total crack length. Although the magnitude of the fluctuations decreases, it is in general not possible to converge to the length of a straight crack unless the mesh is artificially aligned with the anticipated crack path. However, it was found that the simulated crack length is longer

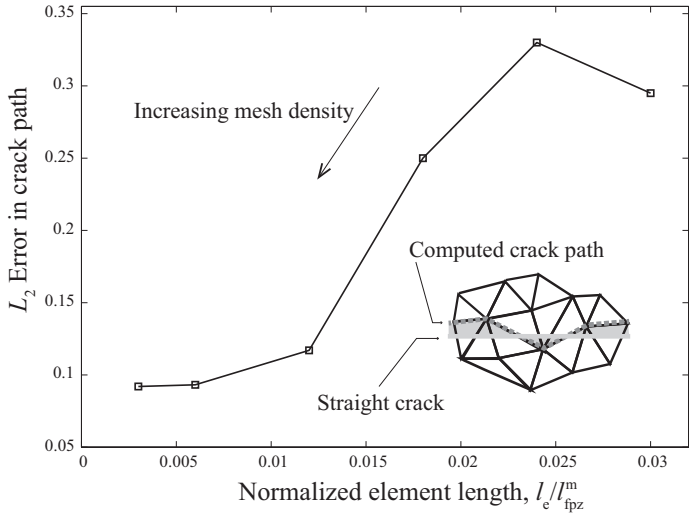

Figure A.18: Error in crack path convergence.

than the ideal straight crack length by only about 4% to 8% in the different mesh densities considered (crack length is calculated by summing up the length of the completely failed cohesive elements). This range of values does not correlate with the mesh density since it is mostly related to a geometrical characteristic of the elements, namely the angle between two edges. Indeed, as can be schematically seen in the inset in Fig. A.18, the error in the length scales with the cosine of the average angle between the straight crack and the fluctuating crack, which is typically between 15° and 25° in the simulations.

As indicated above, mesh dependency with the use of cohesive elements can be significantly mitigated through the use of a sufficiently fine mesh. However, increasing the mesh density not only increases the computational costs, but also it induces an artificial compliance to the system due to the presence of an initial linearly elastic region in the cohesive law. Ideally, the problem of the artificial compliance can be nullified if an initially rigid cohesive law is used. In the present analysis, the rigid behavior is approximated using a sufficiently large stiffness in the cohesive law. Correspondingly, the overall approach adopted here mimics the properties of the XFEM. More importantly, it provides a robust alternative for handling crack coalescence, an issue that still remains elusive within XFEM.